

# Stability of convection in dry salt lakes

Marcel Ernst<sup>\*,1,2</sup>, Jana Lasser<sup>\*,1,3†</sup> and Lucas Goehring<sup>4‡</sup>

\*Shared first author

<sup>1</sup>Max-Planck Institute for Dynamics and Self-Organization, Am Fassberg 17, 37077 Göttingen, Germany

<sup>2</sup>Department of Electrical Engineering and Computer Science, University of Kassel, Wilhelmshher Allee 71 - 73, 34121 Kassel, Germany

<sup>3</sup>Complexity Science Hub Vienna, Josefstädterstrasse 39, 1080 Vienna, Austria

<sup>4</sup>School of Science and Technology, Nottingham Trent University, Nottingham NG11 8NS, UK

Dry lakes covered with a salt crust organised into beautifully patterned networks of narrow ridges are common in arid regions. Here, we consider the initial instability and the ultimate fate of buoyancy-driven convection that could lead to such patterns. Specifically, we look at convection in a deep porous medium with a prescribed fluid flux boundary condition on a horizontal surface, which resembles the situation found below an evaporating salt lake. The system is scaled to have only one free parameter, the Rayleigh number, which characterises the relative driving force for convection. We then introduce a semi-analytical approach to solve the resulting linear stability problem of the onset of convection. Further exploring the non-linear regime of this model with pseudo-spectral numerical methods, we demonstrate that this instability coarsens over time into a dynamical steady state. In this mature state we show how the typical speeds and length-scales of the convective plumes scale with forcing conditions, and the Rayleigh number. Interestingly, a robust length-scale emerges for the pattern wavelength, which is largely independent of the driving parameters. Finally, we introduce a spatially inhomogeneous boundary condition – a modulated evaporation rate – to mimic any feedback between a growing salt crust and the evaporation over the dry salt lake. We show how this boundary condition can introduce phase-locking of the downwelling plumes and compare the simulated phase-locking duration and evaporation rate modulation to field data from a salt lake.

**Key words:** Porous media convection, advection-diffusion, salt polygons, instability, pattern formation

---

## 1. Introduction

This study of porous-media convection is motivated by the patterns shown in Fig. 1. The examples shown there are of dry salt lakes, or playa (Briere (2000)), and are amongst the most inhospitable places on the surface of the earth. Dry lakes typically develop in arid environments, where evaporation outweighs precipitation and where mineral-rich groundwater is refreshed by inflow from surrounding regions of higher altitude (Lowenstein & Hardie (1985); Gill (1996); Briere (2000)). The heat fluxes through the

† Email address for correspondence: jana.lasser@ds.mpg.de

‡ Email address for correspondence: lucas.goehring@ntu.ac.uk

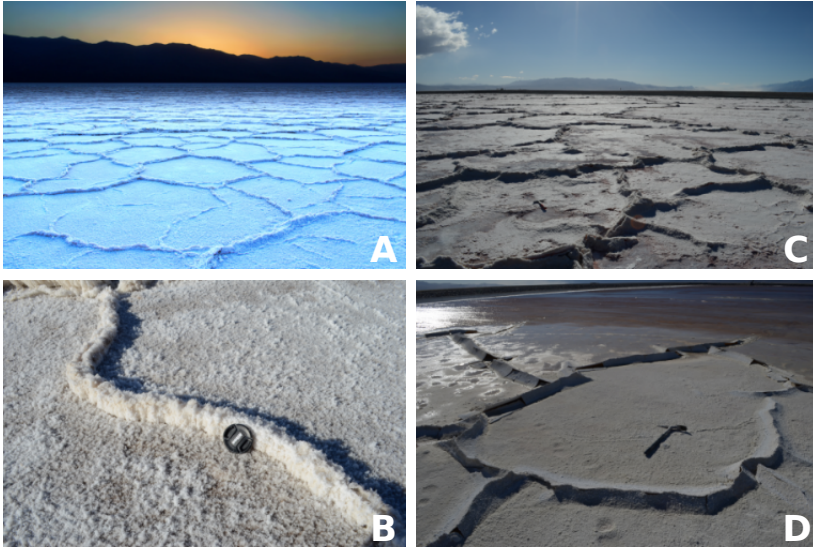


FIGURE 1. Typical salt polygon patterns at (A, B) Badwater Basin in Death Valley and (C, D) Owens Lake, both in California. (Image A courtesy Photographersnature (2012), CC BY-SA 3.0.)

surface of such salt deserts are important to understanding the water and energy balances in arid regions (Bryant & Rainey 2002). Additionally, salt deserts are responsible for a significant part of the global emission of atmospheric dust (Gill 1996; Washington *et al.* 2003; Prospero 2002). However, despite the extreme conditions that prevail above ground, the water table of dry lakes often remains very near to the surface (Gill (1996); Briere (2000); Bryant (2003); Nield *et al.* (2015)), allowing for active patterns of water flows within the pore spaces of the soil (e.g. Wooding *et al.* (1997); Van Dam *et al.* (2009); Tyler *et al.* (1997)). As evaporation rates are high (Tyler *et al.* (1997); Handford (2003); Brunner *et al.* (2004); Groeneveld *et al.* (2010)), soluble salts accumulate in such regions, and precipitate into a solid salt crust covering the desert floor. We have argued recently that these two processes, of subsurface flows and surface crust growth, are coupled together (Lasser *et al.* 2019).

Within the crust of a dry lake, captivating and beautiful patterns can emerge, developing into a network of polygons, as shown in Fig. 1 A. Around the world – from Owens Lake and Badwater Basin in California (Lasser *et al.* (2019)) to the Great Salt Desert of Iran (Krinsley (1970)), Salar de Uyuni in Bolivia and the Sua pan of Botswana (Nield *et al.* (2015)) – these salt polygons are usually expressed with a diameter of a couple meters, individually bounded by ridges a few centimetres high. These regular patterns immediately draw the eye of an observer and the question of their origin arises. The raised structures of polygonal ridge patterns on salt deserts also contributes to surface roughness (Nield *et al.* 2015). Under the effect of the often strong winds which blow over the desert’s surface, dust is emitted from salt pans and is carried into the atmosphere. The surface roughness, alongside the salt chemistry and other crust characteristics, influences the uncertainty in modelling dust emission from the desert’s surface (Raupach *et al.* 1993; Marticorena & Bergametti 1995).

Christiansen (1963) and Krinsley (1970) attempted to explain the growth of salt polygons in dry lakes by the folding and cracking of the salt crust, respectively. However, neither of these explanations is sufficient to explain the emerging polygonal shapes and,

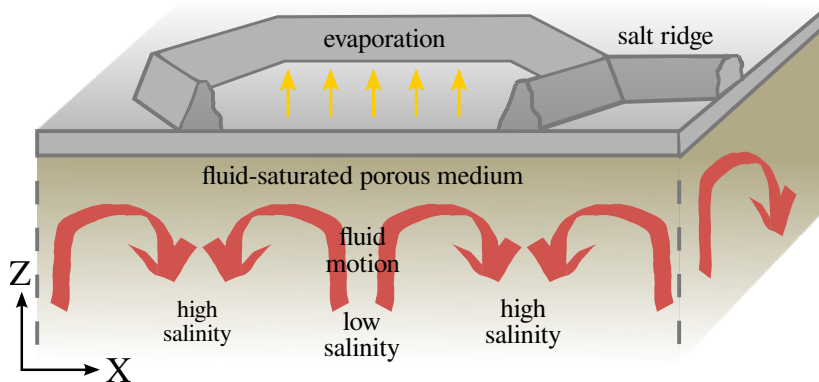


FIGURE 2. Sketch of the proposed buoyancy-driven flows in the soil beneath a polygon: water evaporates at the salt crust (yellow arrows) and a salinity gradient builds up in the fluid-saturated porous medium below. Once the salt-rich boundary layer becomes unstable, fingers of high salinity start sinking downwards below the salt ridges while fresh water rises in the middle of the polygon (red arrows).

in particular, the robust length scale observed in nature around the world. Specifically, both models would predict that the pattern wavelength depends on the thickness of the salt crust. However, this wavelength is consistently 1-3 meters, in crusts ranging from sub-centimetre to several meters thick (Krinsley 1970; Lowenstein & Hardie 1985; ?; Lasser *et al.* 2019). Recently, buoyancy-driven convection, taking place in the porous sand below the patterns, which is filled with salty water, was brought forward as an alternative candidate for a driving mechanism (Lasser *et al.* (2019)). Here, we will model the onset of this mechanism and the scaling of the dynamics of buoyancy-driven convection that can occur below the surface of a dry salt lake.

Specifically, we will present a study of a two-dimensional model of solutal convection in a porous medium, as illustrated in Fig. 2. The porous medium can be interpreted as the sediment below the salt crust of a dry salt lake, and the solute as the salt dissolved in the groundwater that fills the porous medium. The salty groundwater is re-supplied by an influx of moderately saline water from far below. Evaporation of water is enhanced both by wind and high temperatures, causing the precipitation of salt and growth of the crust at the surface. Due to the accumulation of salt near the surface the salinity, and thereby the density, of the water is higher there than it is further below. If the resulting density gradient is large enough this configuration becomes unstable, leading to buoyancy-driven convective motion.

We model this problem in an idealised and simple rectangular geometry, whose domain is chosen to be deeper than it is wide. The domain has an upper boundary that is only permeable to fluid – mimicking fluid loss through evaporation – a lower boundary with a constant flux condition to allow recharge of fluid and periodic boundary conditions in the horizontal direction. Simulations are started with an initial condition in the form of a boundary layer of high salinity, formed just below the top boundary, where salt diffuses into the fluid from the salt crust. This setup is designed to mirror the conditions found below an evaporating salt lake, such as Owens Lake or Badwater Basin. We investigate the onset of convective motion in the system at Rayleigh numbers  $Ra$  close to the critical value,  $Ra_c$ , as well as the behaviour of the dynamics at higher Rayleigh numbers. Here, once the system is appropriately scaled,  $Ra$  is the only free parameter, and can be interpreted as the dimensionless ratio between buoyancy forces and viscous dissipation. As the motivation for this work lies in the connection to pattern-forming processes in

salt deserts, we also investigate the length-scales and time-scales on which coarsening of the dynamics occur, as well as a modulated, non-uniform top boundary condition, which could serve as a connection to feedback processes in nature.

More broadly, we note that the situation of buoyancy-driven convection occurring below an evaporating salt lake is also closely related to the convective overturning of  $\text{CO}_2$ , dissolved in a porous medium filled with brine. This mechanism has become known for its importance to the sequestration of  $\text{CO}_2$  in underground aquifers (e.g. Metz *et al.* (2005); ?); Slim *et al.* (2013); ?); Hewitt *et al.* (2020)) to help mitigate the anthropogenic impact of  $\text{CO}_2$  in the atmosphere. The similarity of models is such that an exchange of methods, insights and results is possible, in both directions. For example, analogous to the study by Slim *et al.* (2013), we numerically investigate the dependence of the dynamics of solutal convection in a porous medium on time, and we find similar regimes of behaviour, from initiation to coarsening and eventually a dynamical steady-state.

The dynamics of thermally-driven porous media convection has also been extensively investigated in the past, for a variety of boundary conditions, and the equations are equivalent to the solutal-driven convection discussed here. Of special interest has been the critical value of the Rayleigh number,  $Ra_c$ , above which the system is unstable to perturbation and convective motion sets in, for a variety of boundary conditions. For example, if perfectly conducting boundary conditions are chosen, similar to the setup of Rayleigh-Bénard convection, then transport of heat across the system is purely conductive for  $Ra < 4\pi^2$  (Horton & Rogers 1945; Lapwood 1948). At higher  $Ra$ , first steady and then perturbed convective rolls occur (Busse & Joseph 1972; Graham & Steen 1994). For  $Ra \gtrsim 1300$ , the dynamics enter a chaotic regime (Otero *et al.* 2004; Hewitt *et al.* 2012).

Thus, there are certain details already known about the onset of convection in the set of equations we study, which we will briefly summarise. For a constant through-flow boundary condition – a situation that resembles a fluid-filled porous medium with surface evaporation at the surface – the onset of instability has been found to be at  $Ra_c \approx 14.35$  (Wooding 1960a; Homsy & Sherwood 1976; van Duijn *et al.* 2002) with a critical wavenumber of  $k_c \approx 0.76$  (Wooding 1960a). Finite amplitude perturbations in the range of  $8.59 < Ra < 14.35$  were also observed to grow in simulations and experiments (van Duijn *et al.* 2002; Wooding *et al.* 1997). In the slightly different case of constant pressure boundary condition at the surface - a situation that resembles an evaporating salt lake covered with brine - the critical values of  $Ra_c \approx 6.95$  and  $k_c \approx 0.43$  are slightly smaller and the system is unstable in a greater range of parameters (Wooding 1960a). Finally, a linear stability analysis (Wooding 1960a) as well as an energy minimisation method (van Duijn *et al.* 2002) were used to calculate the neutral stability curves for both problems, and to determine what range of wavenumbers are unstable at any given  $Ra$ . In what follows we start by reproducing these theoretical results for both boundary conditions using a semi-analytical approach that develops particularly from the work of Wooding (1960a). We are then able to complement the existing analysis by determining the most unstable mode for both constant pressure and constant through-flow boundary conditions, as well as giving the growth rate of an arbitrary mode. This is followed by a numerical study of the ultimate fate of this instability, including its coarsening and scaling in the highly non-linear regime.

## 2. Governing Equations

The dynamics considered are those of fluid flow in the water-saturated porous soil of a dry salt lake and are described by the mass conservation of water and salt, as well

as a detailed momentum balance. The governing equations are those of incompressible flow, the mass conservation of salt with advection and diffusion and Darcy's law (Darcy (1856)) in the presence of gravity and are, respectively,

$$\nabla \cdot \mathbf{q} = 0, \quad (2.1)$$

$$\varphi \frac{\partial S}{\partial t} + \mathbf{q} \cdot \nabla S = \varphi D \nabla^2 S, \quad (2.2)$$

$$\mathbf{q} = -\frac{\kappa}{\mu} (\nabla p + \rho g \hat{\mathbf{z}}). \quad (2.3)$$

These equations describe a fluid of superficial velocity, or flux,  $\mathbf{q}$  and viscosity  $\mu$  passing through a porous medium of porosity  $\varphi$  and permeability  $\kappa$  and carrying with it a dissolved salt of diffusivity  $D$  and relative salinity  $S$ . Flows are driven by a pressure  $p$  and by buoyancy effects due to a gravitational acceleration,  $-g\hat{\mathbf{z}}$ , and evolve over time  $t$ . This system of equations has been studied in a large variety of contexts, including geysers (Wooding 1960a), analogues of Rayleigh-Bénard convection (e.g. Horton & Rogers (1945); Lapwood (1948); Elder (1967); Hewitt *et al.* (2012)), solutal convection (Wooding *et al.* 1997; Boufadel *et al.* 1999) and carbon sequestration applications (e.g. Loodts *et al.* (2014); Hewitt *et al.* (2014)).

The relative salinity  $S$  of the pore fluid depends on its density  $\rho$  and boundary conditions. In our system fluid enters from below ( $z \rightarrow -\infty$ ) at a background density  $\rho_0$  and evaporates as a saturated solution, of density  $\rho_1$ , from the surface at  $z = 0$ . Between these limits

$$S = \frac{\rho - \rho_0}{\rho_1 - \rho_0} = \frac{\rho - \rho_0}{\Delta\rho} \quad (2.4)$$

where  $\Delta\rho = \rho_1 - \rho_0$ . Thus, the salt-saturated fluid in contact with a solid salt crust has a relative salinity of  $S = 1$ , whereas the fluid feeding into the soil from some distant reservoir has  $S = 0$ .

The formulation of Eqs. (2.1)-(2.4) has a number of implicit assumptions. First, it assumes a Boussinesq flow, such that density variations only affect the buoyancy term of Darcy's law. It also neglects the effect of salt concentration on fluid viscosity: Wooding (1960a) has discussed this approximation, and shows how a more realistic salinity-dependant viscosity will produce a small stabilising effect; a similar result was obtained by Boufadel *et al.* (1999), who showed that including a variable viscosity can slightly shift the balance of stability between competing modes of similar wavelengths. Furthermore, the model treats the diffusivity  $D$  as a constant, and thus ignores any velocity-induced dispersion (i.e. Taylor dispersion, (Taylor 1953)). Wooding *et al.* (1997) show how to consider such effects, but for the field conditions measured at the salt playa of Owens Lake (Lasser *et al.* 2019; Lasser 2019) these should be negligibly small. Finally, the equations treat the porosity and permeability of the soil as constant in space and time. For exemplary research on systems with heterogeneous permeability or porosity, see Chen & Meiburg (1998b); Sharp & Shi (2009); Li *et al.* (2019); Hewitt *et al.* (2019); and Harfash (2013), respectively.

The non-dimensionalisation of our problem requires choosing a characteristic length  $L$  and velocity (i.e. flux)  $V$ . A natural time-scale then follows as  $T = \varphi L/V$ . Generally, for problems in porous media convection, scaling results in one of two clear choices for

dimensionless groups, as Eqs. (2.2) and (2.3) become

$$\frac{\partial S}{\partial \tau} + \mathbf{U} \cdot \nabla S = \frac{\varphi D}{LV} \nabla^2 S, \quad (2.5)$$

$$\mathbf{U} = -\nabla P - \frac{\kappa \Delta \rho g}{\mu V} S \hat{\mathbf{Z}}, \quad (2.6)$$

where  $\mathbf{U} = \mathbf{q}/V$ ,  $\tau = t/T$ ,  $Z = z/L$  and  $P$  is an appropriately rescaled pressure. For example, applications in carbon sequestration often use the limiting speed at which a dense parcel of fluid falls,  $V_B = \kappa \Delta \rho g / \mu$ , as a natural velocity scale (Slim 2014; Hewitt *et al.* 2014, 2020). In other cases a slab geometry of fixed height is modelled, in which case a scaling based on the layer thickness is sometimes made (Riaz & Meiburg 2003; Ruith & Meiburg 2000).

We will focus on the situation of a solid salt crust, through which there is a constant and uniform evaporation; the more complex case of a modulated evaporation rate will be explored in Section 5. As a boundary condition at the surface the upward fluid flux must balance evaporation, i.e  $V = E$  at  $z = 0$ . This will also give the average vertical velocity of the pore fluid anywhere within the soil. Now the governing equations allow for a simple steady-state solution,

$$S(z) = e^{zE/\varphi D}, \quad (2.7)$$

which represents a dense boundary layer of fluid near the crust. Following Wooding (1960*a*), we therefore use  $L = \varphi D/E$  as the characteristic thickness of the heavy boundary layer which can develop. This natural length is also the distance over which advective and diffusive effects will be of comparable magnitude. The natural timescale  $T = \varphi^2 D/E^2$  is then the time fluid takes to cross the boundary layer, in the steady state. Applying these transformations results in the following non-dimensional formulation of Eqs. (2.1)-(2.3),

$$\nabla \cdot \mathbf{U} = 0, \quad (2.8)$$

$$\frac{\partial S}{\partial \tau} + \mathbf{U} \cdot \nabla S = \nabla^2 S, \quad (2.9)$$

$$\mathbf{U} = -\nabla P - Ra S \hat{\mathbf{Z}}, \quad (2.10)$$

which is controlled by the Rayleigh number

$$Ra = \frac{\kappa \Delta \rho g}{\mu E}. \quad (2.11)$$

Here,  $Ra = V_B/E$  also represents the ratio of the characteristic speeds of a fluid parcel due to buoyancy and evaporation. Finally, we note that the rescaled pressure,

$$P = \frac{\kappa}{\varphi \mu D} (p + \rho_0 g z),$$

is now defined to include a contribution from the background fluid density.

In the rescaled system the boundary conditions are  $U_Z = S = 1$  at  $Z = 0$  (where  $U_i$  are the components of  $\mathbf{U}$ ), with the salinity approaching the limit  $S = 0$  at large depths. These conditions are appropriate as long as there is no significant ponding of surface water (Wooding *et al.* 1997; van Duijn *et al.* 2002), and are analogous to the thermal problems studied by Wooding (1960*a*); Homsy & Sherwood (1976). The steady-state solution has  $\mathbf{U} = (0, 0, 1)$  everywhere, a salinity boundary layer given by  $S = e^Z$  and a corresponding pressure  $P = Ra(1 - e^Z) - Z$ . We now turn to investigate the stability of this steady-state.

### 3. Linear Stability Analysis

We now perform a linear stability analysis of our model for small perturbations in an infinite half-space ( $Z \leq 0$ ) of a three-dimensional porous medium saturated with saline water evaporating at the top boundary with constant evaporation rate  $E$ , and recharged from below by a reservoir of constant salinity water. These methods are inspired by those used by Wooding (1960*a*), but extend the results to an analytic series solution to the problem.

In order to investigate the stability of the steady-state solution we add small perturbations  $\tilde{\mathbf{U}}$ ,  $\tilde{S}$ ,  $\tilde{P}$  to the velocity, salinity and pressure, respectively. To leading order (i.e. ignoring the  $\tilde{\mathbf{U}} \cdot \nabla \tilde{S}$  term) these perturbations will grow or decay according to

$$\nabla \cdot \tilde{\mathbf{U}} = 0, \quad (3.1)$$

$$\frac{\partial \tilde{S}}{\partial \tau} + \frac{\partial \tilde{S}}{\partial Z} + \tilde{U}_Z e^Z - \nabla^2 \tilde{S} = 0 \quad (3.2)$$

$$\tilde{\mathbf{U}} + \nabla \tilde{P} + Ra \tilde{S} \hat{\mathbf{Z}} = 0. \quad (3.3)$$

The pressure term can be eliminated by taking the curl of Eq. (3.3), as  $\nabla \times (\nabla \tilde{P}) = 0$ . By applying the curl twice, simplifying with Eq. (3.1) and considering the  $Z$ -component of the result, one finds that Eq. (3.3) implies that

$$\nabla^2 \tilde{U}_Z + Ra (\partial_X^2 + \partial_Y^2) \tilde{S} = 0. \quad (3.4)$$

To respect the boundary conditions,  $\tilde{U}_Z = \tilde{S} = 0$  at  $Z = 0$ . As we can assume a steady state flow far from the unstable surface layer, the vertical perturbation of velocity must decay to zero as  $Z \rightarrow -\infty$ . Rearranging eq. (3.2) gives

$$\tilde{U}_Z = e^{-Z} \left( \nabla^2 \tilde{S} - \frac{\partial \tilde{S}}{\partial Z} - \frac{\partial \tilde{S}}{\partial \tau} \right), \quad (3.5)$$

which also implies (Wooding 1960*b*) that

$$e^{-Z} \frac{\partial \tilde{S}}{\partial Z} \rightarrow 0 \quad \text{for } Z \rightarrow -\infty. \quad (3.6)$$

Now we use the instability  $\tilde{S}(X, Y, Z, \tau)$  following the approach of Pellew & Southwell (1940) as well as Wooding (1960*a*) assuming separation of variables

$$\tilde{S}(X, Y, Z, \tau) = F(Z) \Phi(X, Y) e^{\alpha \tau}. \quad (3.7)$$

We assume that  $\Phi$  is a harmonic function  $\Phi = \Phi(X, Y)$  which satisfies the condition  $(\partial_X^2 + \partial_Y^2 + k^2) \Phi(X, Y) = 0$ , where  $k$  is the characteristic wavenumber of the perturbations in horizontal  $X$ - and  $Y$ -directions and  $\alpha$  its non-dimensional growth rate. For  $\alpha > 0$  the amplitude of the perturbation increases and hence the system is unstable and for  $\alpha < 0$  the perturbation decays and the system is stable.

Using eq. (3.5) we plug in the perturbation eq. (3.7) in eq. (3.4) to get the eigenvalue equation for the non-dimensional height-dependence  $F(Z)$

$$(\partial_Z^2 - k^2 + 1) (\partial_Z^2 - \partial_Z - k^2 - \alpha) F(Z) = k^2 Ra e^Z F(Z). \quad (3.8)$$

According to the relation for the Rayleigh number eq. (2.11) the system is only affected by gravitational instability. Following eq. (3.5) we introduce

$$G(Z) := [\partial_Z^2 - \partial_Z - k^2 - \alpha] F(Z) \quad (3.9)$$

and get the boundary condition  $G(0) = 0$  since  $\tilde{U}_Z(Z=0) = 0$ . Besides we have  $F(0) = 0$  since  $\tilde{S}(Z=0) = 0$ . Wooding (1960a) solved an equivalent equation for the case of neutral stability ( $\alpha = 0$ ) where we are giving the general series solution for  $\alpha \neq 0$  as well.

Using `DSolve` in `Mathematica` we obtain an analytical solution of the differential equation (3.8) operating on  $F(Z)$ . The solution is a superposition of four independent infinite series solutions. With  $\Psi := \sqrt{1 + 4k^2 + 4\alpha}$  and

$$\begin{aligned} c_{0/1} &= 1 \pm k \\ c_{2/3} &= \frac{1}{2} \left( 1 \pm \sqrt{1 + 4(k^2 + \alpha)} \right) = \frac{1}{2} (1 \pm \Psi) \end{aligned}$$

the solutions read

$$F_i(Z) = (-k^2 Ra e^Z)^{c_i} H_i(Z) \quad \text{for } i \in \{1 \dots 4\} \quad (3.10)$$

where  $H_i(Z)$  is defined by

$$\begin{aligned} H_{0/1}(Z) &= \sum_{n=0}^{\infty} \left[ (-k^2 Ra e^Z)^n \left( n! \prod_{j=0}^{n-1} (2c_{0/1} - 1 - j) \left( \left( c_{0/1} + \frac{1}{2} - j \right)^2 - \frac{\Psi^2}{4} \right) \right)^{-1} \right], \\ H_{2/3}(Z) &= \sum_{n=0}^{\infty} \left[ (-k^2 Ra e^Z)^n \left( n! \prod_{j=0}^{n-1} (2c_{2/3} - j) \left( (c_{2/3} - j)^2 - k^2 \right) \right)^{-1} \right]. \end{aligned}$$

$H_i(Z)$  are basic hypergeometric series  ${}_rF_s(Z)$  with  $r = 0$  and  $s = 2$  (Koekoek & Swarttouw 1998, p. 12). Since  $r < s + 1$  the convergence radius is  $\infty$  for  $H_i(Z)$  only if the denominator never is 0 (Koekoek & Swarttouw 1998, p. 12) which is fulfilled if  $(\frac{1}{2} + \frac{\Psi}{2} - k), \Psi \notin \mathbb{N}$  and  $(\frac{\Psi}{2} + k) \neq \frac{3}{2}$  and therefore a dense set in the  $k, \Psi$ -space. Hence, we assume  $H_i(Z)$  to converge for  $Z \rightarrow -\infty$ .

Due to equation (3.6) we know that  $F(Z)$  has to decay faster than  $e^Z$  for  $Z \rightarrow -\infty$ . Hence, we only consider the  $F_i(Z)$  fulfilling the condition that  $c_i$  are larger than 1 since  $F_i(Z) \propto e^{Z c_i}$ . Since  $k > 0$  as well as  $\alpha \geq 0$  and hence  $\Psi \geq \frac{1}{2} + k$  we know that  $c_2 = \frac{1}{2}(1 + \Psi) > 1$ ,  $c_0 = 1 + k > 1$  and  $c_1, c_3 < 1$ .

Hence, we only superpose the two solutions for  $c_0$  and  $c_2$ . The top boundary conditions can be satisfied with non-zero constants if and only if  $F(0) = G(0) = 0$  using eq. (3.9) with  $F(0) = C_0 F_0(0) + C_2 F_2(0)$  and  $G(0) = C_0 G_0(0) + C_2 G_2(0)$  and  $C_0, C_2 \in \mathbb{R}$ . Consequently, we know that either  $C_0 = C_2 = 0$  or

$$\Delta(Z)|_{Z=0} = \begin{vmatrix} F_0(Z) & F_2(Z) \\ G_0(Z) & G_2(Z) \end{vmatrix}_{Z=0} = F_0(0) G_2(0) - F_2(0) G_0(0) = 0.$$

Since only the non-zero solution is physically relevant we are applying this relation at the top boundary to get a relation between  $Ra$ ,  $k$  and  $\alpha$ . Based on the solutions  $F_0(Z)$  and  $F_2(Z)$  in eq. (3.10) we can compute  $\Delta(0)$  and use `FindRoot` for fixed values of  $k$  and  $\alpha$  to find the smallest  $Ra > 0$  satisfying the boundary condition.

Wooding (1960a) applies different top boundary conditions which are corresponding constant salinity  $S = 1$  and constant pressure instead of constant through-flow. Using eq. (3.3) it follows that the central term and the  $X/Y$ -components of the velocity perturbation  $\tilde{\mathbf{U}}$  vanish and only the  $Z$ -component  $\tilde{U}_Z$  remains. Equation (3.1) directly yields in that case

$$\partial_Z \tilde{U}_Z \Big|_{Z=0} = 0. \quad (3.11)$$

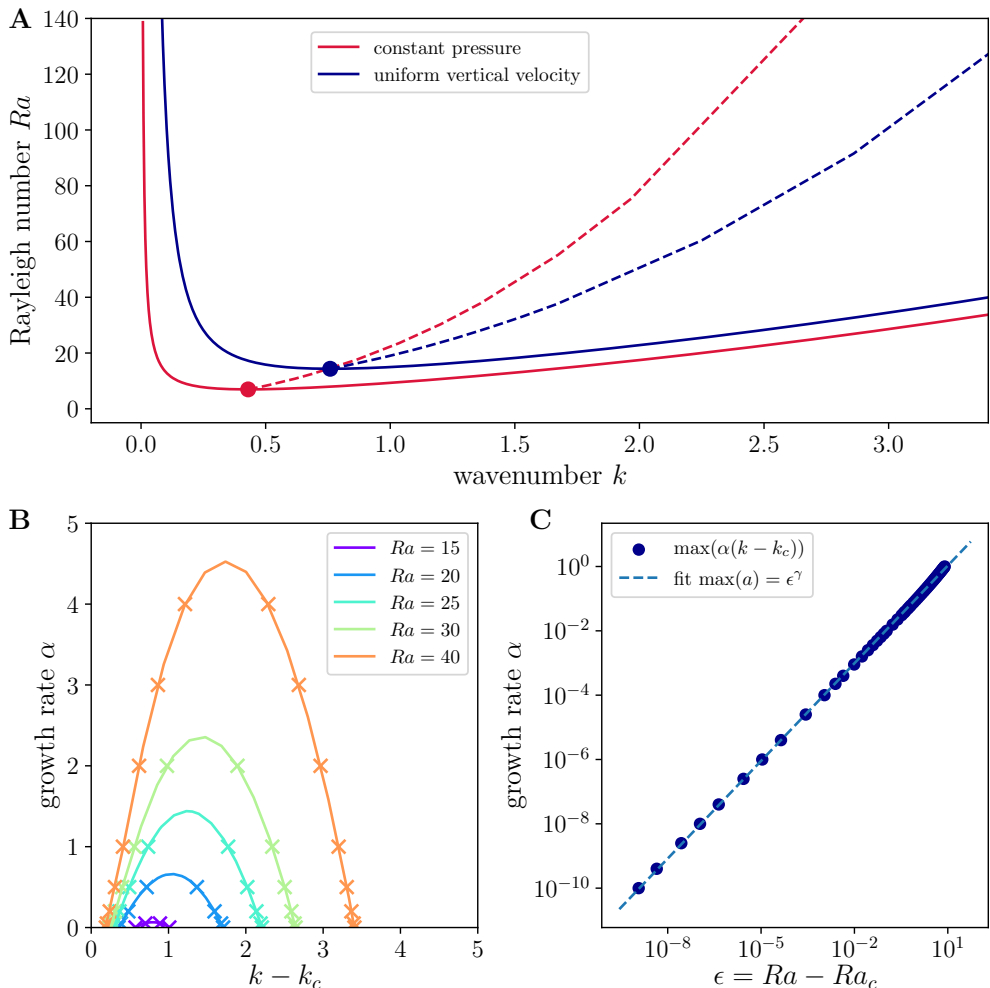


FIGURE 3. **A** Neutral stability curves  $Ra(k)$  (solid lines), critical points  $Ra_c$ ,  $k_c$  (circles) and the most unstable mode (dashed lines) according to the linear stability analysis with constant salinity at the top and either constant pressure  $P$  (red) or uniform vertical velocity  $w = 1$  (blue). **B** Theoretical prediction of growth rates  $\alpha$  over wavenumber  $k - k_c$  (solid lines) for a selection of  $Ra$  close to the onset of instability. Measurements from simulations are indicated as crosses. **C** The growth rate of the most unstable mode follows a power law  $\max(\alpha) = \epsilon^\gamma$  which deviates from  $\gamma = 1$  if  $\epsilon \gg 0$ .

The derivation is analogous except for the definition of  $G(Z)$ :

$$G(Z) := (\partial_Z [e^{-Z} (\partial_Z^2 - \partial_Z - k^2 - \alpha)] F(Z)) \quad (3.12)$$

In figure 3 **A** we display the neutral stability curve and the critical points for both types of boundary conditions at the surface: constant pressure  $P$  (red) or uniform vertical velocity  $U_Z$  (blue), corresponding to a uniform evaporation rate  $E(X, Z, \tau) = E_0$ . We calculated the relation between the Rayleigh number  $Ra$  and the wavenumber  $k$  for a growth rate  $\alpha = 0$ . The critical points at  $Ra_c$  and  $k_c$  of the neutral stability curves are given in table 1.

The numerical values of the neutral stability curve with constant pressure are equal to

---

Boundary condition	$Ra_c$	$k_c$
constant pressure	6.954	0.429
uniform flow rate	14.35	0.7585

---

TABLE 1. Critical wavenumber  $k_c$  and Rayleigh number  $Ra_c$ .

the results of Wooding (1960*a*). The critical point, as well as the neutral stability curve, is equivalent to the results of Homsy & Sherwood (1976) and van Duijn *et al.* (2002) who solved the same problem using different approaches.

As shown in fig. 3 **B**, our numerical results (crosses) measured for different  $Ra$  perfectly match the theoretical prediction for  $\alpha(k)$ . We also investigate how the growth rate of the most unstable mode  $\max(\alpha)$  scales with  $\epsilon = Ra - Ra_c$ . As expected (Cross & Greenside 2009, p. 221), the growth rate of the most unstable mode obeys a power law with a slope of  $\gamma = 1$  as  $\epsilon \rightarrow 0$  (fig. 3 **C**). For  $\epsilon \gg 0$ ,  $\gamma$  increases.

#### 4. Scaling relations

In the following, we will investigate the scaling of the dynamics in time and space. To study the dynamics, we numerically solve the governing equations (2.8) to (2.10), following the approaches described by Riaz & Meiburg (2003); Ruith & Meiburg (2000); Chen & Meiburg (1998*a*). Details about the implementation of the simulations can be found in the Appendix, snapshots of an exemplary simulation at  $Ra = 100$  and at different times  $\tau$  are displayed in fig. 4. We simulate ensembles of 5 to 10 runs at every Rayleigh number for a selection of Rayleigh numbers, ranging from  $2 \cdot 10^1$  to  $2 \cdot 10^3$ .

Similar to Slim (2014) we find several regimes of the dynamics: After the onset of the instability, we observe a regime of linear growth of high salinity fingers fig. 4 **B** and **C**. This is followed by the flux-growth regime, where the downwelling fingers start stripping the boundary layer of solute, fig. 4 **D** and **E**. As a consequence, the boundary layer becomes thinner. The fourth regime is the merging regime, where fingers start influencing each other via long-range interactions in the horizontal velocity field, fig. 4 **F** and **G**. As a result, fingers zip together and form larger plumes. As the fingers have merged, the high salinity boundary layer feeding the plumes starts to grow again, until small proto-plumes start emerging at the top boundary again, which we call re-initiation regime, fig. 4 **H**. These proto-plumes move horizontally until they are swept into the mega-plumes.

We do not see a diffusive regime at the very start of the simulations since we start with an initial condition that reflects the steady state salinity distribution  $S^0(Z) = e^Z$ , as stated above, which is immediately unstable. We also do not observe a shut-down regime since we usually terminate simulations before the absolute salinity in the domain reaches high enough values.

##### 4.1. Velocity

The dynamics evolve faster, the higher the Rayleigh number is (see supplementary videos S1, S2 and S3 for three example simulations at  $Ra = 30$ ,  $Ra = 100$  and  $Ra = 1000$ ). We can quantify the system velocity by calculating the velocity magnitude at every time step  $\tau_i$  of a simulation:

$$V(\tau_i) = |\max(U_Z(X, Z, \tau_i)) + \widehat{Z}|$$

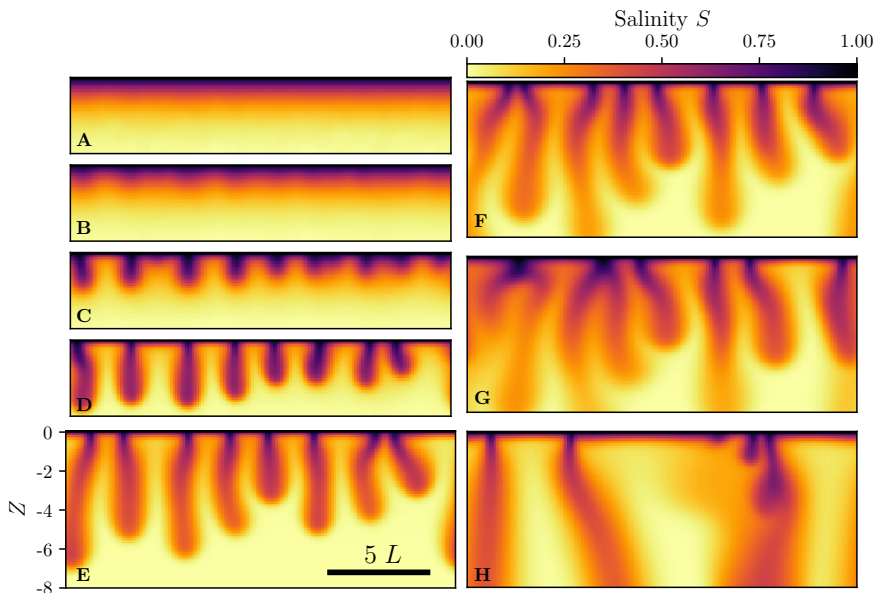


FIGURE 4. Snapshots of simulated concentration profiles at different times  $\tau$  for  $Ra = 100$ . **A** Initial salinity distribution at  $\tau = 0.01$ , linear growth **B**  $\tau = 0.1$ , linear growth **C**  $\tau = 0.2$ , flux growth **D**  $\tau = 0.3$ , flux growth **E**  $\tau = 0.5$ , merging **F**  $\tau = 0.75$ , merging **G**  $\tau = 1.0$ , re-initiation **H**  $\tau = 2.25$

To compare the velocities at different  $Ra$  we re-scale time by a factor  $1/(Ra - Ra_c) = 1/\epsilon$  and use  $\hat{\tau} = \tau \cdot \epsilon$ . This re-scaling will be used in the rest of this work.

In fig. 5 **A**, the time development of  $V(\tau)$  is displayed for a range of Rayleigh numbers: the velocity increases at first until it reaches a maximum velocity and then approaches a constant value. The initial increase of the velocity corresponds to the linear growth, flux-growth and merging regimes whereas the constant velocity corresponds to the re-initiation regime, which seems to be a dynamical steady state.

For  $Ra > 10^2$  the velocity overshoots significantly, as can be seen in fig. 5 **B** for an exemplary simulation at  $Ra = 10^3$ . As the shutdown regime approaches, the velocity decreases again. For every  $Ra$  we identify the maximum velocity  $V_{\max}$  (blue dot in fig. 5 **B**). We determine the beginning of the dynamical steady state  $\tau_{\text{stst}}$  as the time after which  $\frac{\partial V(\hat{\tau})}{\partial \hat{\tau}} < 0.1$  and therefore the velocity in the system does not increase or drop significantly anymore (grey dashed line in fig. 5 **B**). As shown in fig. 5 **C**,  $\tau_{\text{stst}}$  depends on  $Ra$  for  $Ra \leq 500$  and then approaches a constant value of  $\tau_{\text{stst}} \approx 40 \hat{\tau}$ . This can be explained by the time the initial perturbations need to grow, since the amplitude of the perturbations in the initial condition of the salinity field is chosen to be independent of  $Ra$ .

We can calculate the steady state velocity as the mean velocity in the window between  $\tau > \tau_{\text{stst}}$  and  $\tau < \tau_{\text{stst}} + 100 \hat{\tau}$ . The window and  $\tau_{\text{stst}}$  are indicated as the transparent grey area and the red dashed line in fig. 5 **B** respectively. The window is chosen such that for large  $Ra$  - where the shut-down regime approaches faster - it does not include the shut-down regime while spanning enough time to yield a stable mean value for  $V_{\text{stst}}$ .

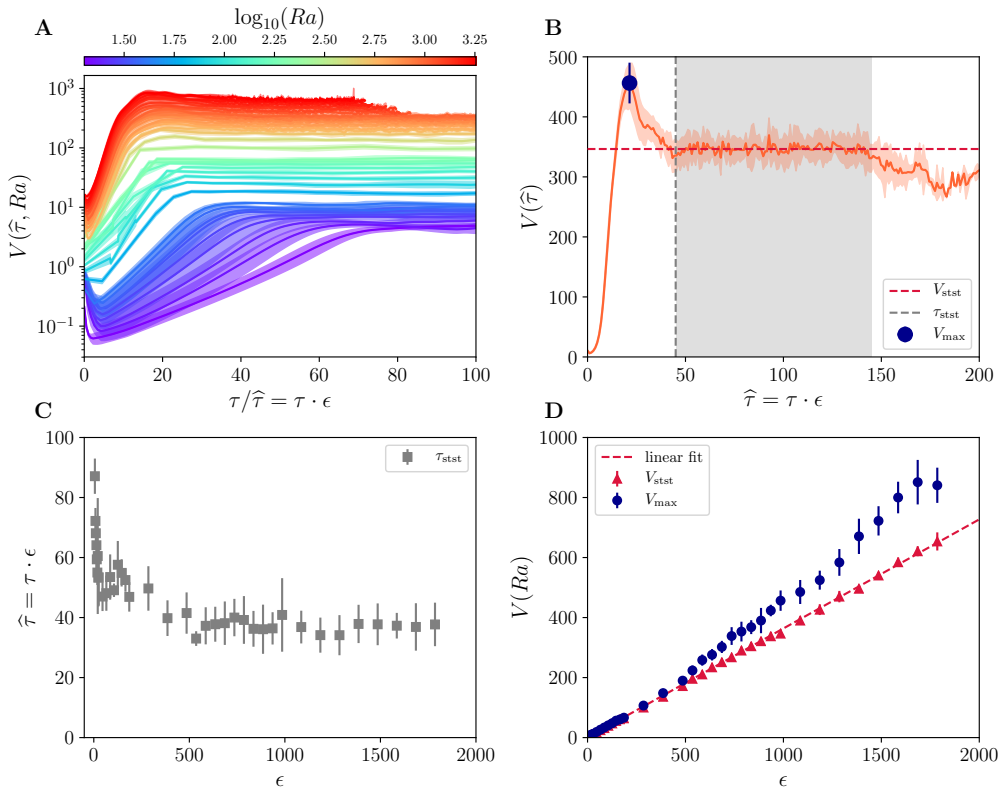


FIGURE 5. Development of the system velocity  $V$  with re-scaled time  $\hat{\tau}$  and  $Ra$  and  $\epsilon = Ra - Ra_c$  respectively. **A** Velocities for simulations spanning three decades of  $Ra$  - note the logarithmic colour scale. **B** The velocity development with  $\hat{\tau}$  for an exemplary ensemble at  $Ra = 1000$ . The blue dot, red dashed line, grey dashed line and grey area indicate the measured maximum velocity  $V_{\max}$ , the dynamical steady state velocity  $V_{\text{stst}}$ , the beginning of the dynamical steady state  $\tau_{\text{stst}}$  and the time period used to calculate  $V_{\text{stst}}$  respectively. **C** Time  $\tau_{\text{stst}}$  until the dynamical steady state is reached for a range of  $Ra$ , **D** Development of  $V_{\max}$  and  $V_{\text{stst}}$  with  $Ra$ .

In fig. 5 **D**, we show that both  $V_{\max}$  and  $V_{\text{stst}}$  increase linearly with  $Ra$ . The velocity in the system is an indicator of how fast the dynamics undergo the different regimes.

#### 4.2. Plume wavelength

As the system changes from regime to regime, the number of fingers and plumes decreases and the dynamics coarsen. In the following, we will quantify this coarsening behaviour with the aim of explaining the characteristics of systems that are far away from the onset in time.

To characterise the state of the dynamics in a simulation at a given depth  $Z_i$  and time  $\tau_i$ , we define the wavelength  $\Lambda(Z_i, \tau_i) = W/N$  of the system, where  $W$  is the width of the simulated domain and  $N$  is the number of downwelling plumes of high salinity. Downwelling plumes are identified as maxima in the salinity distribution  $S(X, Z_i)$ . We define the corresponding wavenumber  $k(Z_i, \tau_i) = 2\pi/\Lambda(Z_i, \tau_i)$ .

In fig. 6 **A** we show the time development of the wavenumber  $k$  for an exemplary simulation run at  $Ra = 100$  and different depths  $Z_i$ . The different regimes of the dynamics described above are reflected in the development of the wavenumber: In the linear-growth regime at  $Z = -1$  and  $\tau < 10\hat{\tau}$ , the wavenumber matches the theoretical prediction

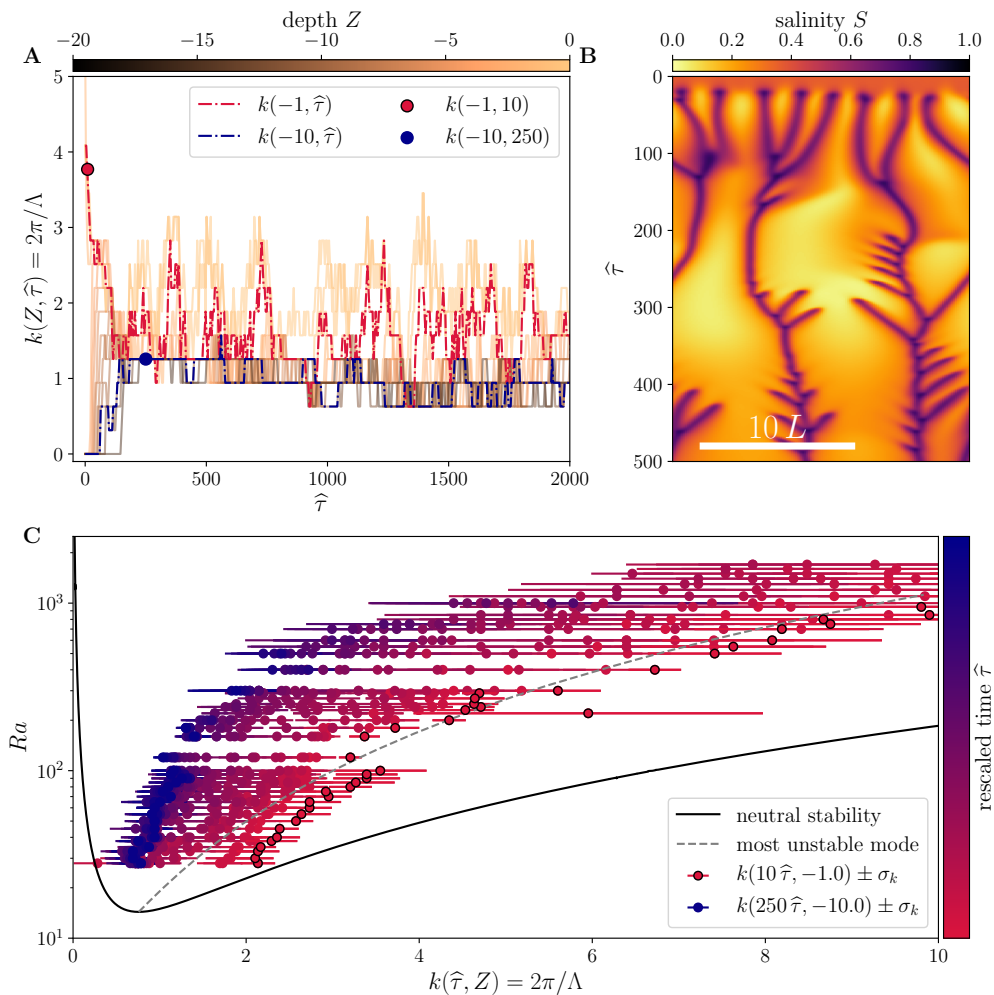


FIGURE 6. **A** Exemplary time-development of a simulation at  $Ra = 100$ . **A** Wavenumber  $k$  measured at different depths  $Z$ . Indicated as red dashed line is the wavenumber development for  $k(-1, \hat{\tau})$  close to the top boundary and close to onset of the instability. Indicated as blue dashed line is the wavenumber development for  $k(-10, \hat{\tau})$ , removed from the top boundary and after onset of the instability. The two dots indicate the wavenumbers measured for this  $Ra$  at  $10\hat{\tau}$  and  $250\hat{\tau}$  respectively, which are also displayed in panel **C**. **B** Space-time diagram of the simulation recorded at  $Z = -1$ . Note that the time only includes values up to  $500\hat{\tau}$ . **C** Wavenumbers measured in simulations for different  $Ra$  in the range of  $Ra = 30$  to  $Ra = 2000$  and at different times between  $10\hat{\tau}$  and  $250\hat{\tau}$ .

closely (see fig. 3 **A** at  $Ra = 100$ ). In the region  $10\hat{\tau} \leq \tau < 150\hat{\tau}$ , the flux growth regime, the wavenumber declines sharply. From  $\tau \geq 150\hat{\tau}$  onward the wavenumbers in the region  $Z < -10$  approach a rather stable value of  $k \approx 1.2$  (blue dashed line in fig. 6 **A**). The wavenumber in the region  $Z > -10$ , close to the top boundary (red dashed line in fig. 6 **A**), oscillates between that stable value and a much higher value of  $k \approx 3$  - which is indicative of the re-initiation stage. We conclude that the dynamics of the system coarsen both with time and depth. The re-initiation and merging of fingers also becomes apparent in the space-time diagram of the simulation displayed in fig. 6 **B**.

In the following, we want to further quantify how far the coarsened dynamics deviate

from the theoretical prediction of the wavenumber at the onset. To this end we trace the development of wavenumbers measured close to the onset (red dot in fig. 6) as the system enters the dynamical steady state (blue dot in fig. 6). We chose to measure wavenumbers in the dynamical steady state at a depth of  $Z = -10$ , since at this time almost all of the plumes will have merged and the wavenumber is more stable than the wavenumber measured close to the top boundary. As can be seen when comparing the wavenumber development at  $Z = -1$  and  $Z = -10$  in fig. 6 **A** (red and blue dashed line respectively), the wavenumber measured at  $Z = -10$  traces the minima of the wavenumber measured at  $Z = -1$ .

The results for a range of Rayleigh numbers between  $Ra = 3 \cdot 10^1$  and  $2 \cdot 10^3$  are shown in fig. 6 **C**. The wavenumbers measured close to onset (red dots with black frame) closely follow the theoretical prediction for the most unstable mode (grey line). As the system ages, the dependence on  $Ra$  weakens (purple and blue dots). Nevertheless, all measured wavenumbers stay within the bounds set by the neutral stability line (black line in fig. 6 **C**).

#### 4.3. Salinity distribution and boundary layer

The emergence of plumes in the system is driven by the ubiquity of salt in the diffusive boundary layer below the top boundary. Therefore a closer look at the time-development of the width of this layer  $L'$  is warranted. In the steady-state solution, the shape of the salinity distribution  $S(Z, X)$  is characterised by eq. (2.7) where  $L' = 1$  by definition. So far, all our simulations were started with a salinity distribution with an initial depth of  $L^0 = 1$  (subsequently also called "initial condition"). Nevertheless, after the onset of instability, the depth of the boundary layer quickly shrinks and oscillates around a value of  $L' < 1$  in the dynamical steady state, which is also dependent on the  $Ra$  of the system. These oscillations are linked to the emergence of proto-plumes at the top boundary.

In fig. 7 **A** we show the horizontally averaged salinity distribution  $\langle S(Z) \rangle$  in the dynamical steady-state for a range of  $Ra$ : After the initial exponential decay of salinity with depth, for higher  $Ra$  the salinity reaches a local maximum around  $S \approx 0.3$  for  $Ra \geq 300$ . For  $Ra < 300$ , the salinity approaches a constant value below a depth of  $Z \approx -2$ . As the domain is finite in  $Z$ -direction, for high  $Ra$  (red) salinity starts building up below  $Z \approx -9$  since the bottom boundary of the simulated domain is at  $Z = -10$ .

To quantify the depth of the diffusive boundary layer at a point  $\hat{\tau}_i$  in time, we fit an exponential decay function  $f(Z) = c_1 \cdot \exp(Z/L') + c_2$  to the rapidly decaying part of the salinity distribution below the top boundary. In fig. 7 **A** (inset) the salinity at grid points  $Z_i$  with spacing  $\Delta Z$  (circles) and corresponding fits (solid lines) for a selection of representative  $Ra$  are shown.  $\Delta Z$  is the resolution of the simulation and is chosen differently for different  $Ra$ , ranging from  $\Delta Z = 1/8$  at  $Ra = 20$  to  $\Delta Z = 1/80$  at  $Ra = 2000$ . Only filled circles were included in the fit. This was done because, after the initially sharp salinity decay, the salinity distribution deviates from an exponential form and shows a "bump", which is expressed more strongly for higher  $Ra$ .

In fig. 7 **B** the development of  $L'(\hat{\tau})$  with re-scaled time  $\hat{\tau}$  is shown for a selection of  $Ra$ . The layer thickness oscillates over time and oscillations correspond to the emergence of proto-plumes. Mean layer thickness (dashed lines) and oscillation amplitudes decrease with increasing  $Ra$  and oscillation periods increase respectively. Therefore the speed at which the system changes between a state with a few large plumes and the emergence of proto-plumes scales faster with  $Ra$  than the overall system velocity in the dynamical steady state.

In fig. 7 **C** we show a time-averaged  $L'$ , re-scaled by  $\epsilon/Ra_c$ . It is apparent that the re-scaled layer thickness increases until  $Ra \approx 400$  and then assumes a constant value of

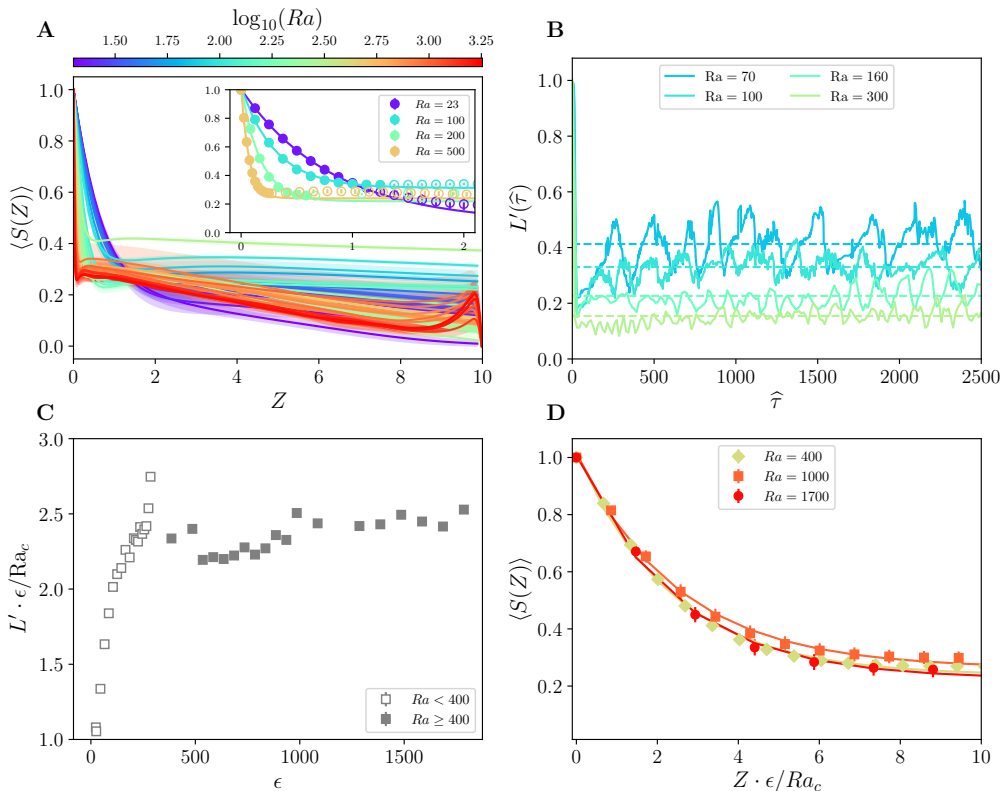


FIGURE 7. Dependence of salinity distribution  $S(Z)$  and boundary layer thickness  $L'$  on  $Ra$  and rescaled time  $\hat{\tau}$ . **A**: Salinity distributions and exponential fits (inset) in the dynamical steady state for a range of  $Ra$ . Salinity distributions were averaged over the  $X$ -axis and over 5-10 ensembles for every  $Ra$ . Note the logarithmic colour scale for  $Ra$ . **B** Layer thickness  $L'$  over time determined by exponential fits to the salinity distribution. Every line corresponds to a single simulation run for a selection of  $Ra$ . The color scale is the same as in panel **A**. **C** Dependence of rescaled layer thickness  $L' \cdot \epsilon / Ra_c$  on  $\epsilon$ .  $L'$  was measured as in panel **B** and subsequently averaged over at least one oscillation period in the dynamical steady-state. **D** Salinity distribution over the rescaled length  $Z \cdot \epsilon / Ra_c$  for a selection of  $Ra > 400$ . The colour scale is the same as in panel **A**.

$L' \cdot \epsilon / Ra_c \approx 2.4$ . If we re-scale the salinity distributions  $S(Z)$  by the same factor (as shown in fig. 7 **D** for a selection of  $Ra > 400$ ), the distributions collapse.

Our simulations are started with a prescribed initial width of the salinity boundary layer  $S(\hat{\tau} = 0, Z) = \exp(Z/L^0)$  of  $L^0 = 1$ . The depth of the boundary layer is far larger than needed for the onset of instability. This can also explain the significant velocity overshoot shown in fig. 5 **B**: the excess salinity in the top boundary layer falls down quickly and reduces the thickness of the boundary layer. As the system reaches a dynamical steady-state, the depth of the boundary layer will be balanced by the diffusive flux of salinity into the layer from the top boundary and the advective removal of salinity by down moving proto-plumes. Therefore, as time passes, the salinity distribution becomes steeper, as shown in fig. 8 **A** for an exemplary initial condition of  $L^0 = 1$ .

To investigate, how the initial dynamics of the system unfold until it reaches the dynamical steady-state, we varied the depth of the boundary layer used as initial salinity distribution between  $L^0 = 0.1$  and  $L^0 = 1.0$ . As in our investigation of the behaviour of

the boundary layer for different  $Ra$  (fig. 7), we fit an exponential decay function to the first part of the salinity distribution to determine the current width of the boundary layer  $L'(\hat{\tau})$ . In fig. 8 **B** we show the development of  $L'(\hat{\tau})$  for a selection of initial conditions  $L_i^0$  at early times. It is clearly visible that for  $L^0 < 1$ , the boundary layer first grows and then shrinks again, as the instability sets in. Surprisingly, the maximum value of  $L'(\hat{\tau})$  depends on the initial width of the boundary layer, which is indicative of a competition between the growth of the boundary layer and the growth rate of the most unstable mode.

The maximum value of  $L'(\hat{\tau})$ , as well as the time it takes until the maximum value is reached, will also depend on the amplitude of the initial noise in the system. At the start of a simulation, we seed the initial salinity distribution with additive noise with a maximum amplitude of  $\eta$ . In fig. 8 **C** we show the time development of  $L'$  at  $L^0 = 0.4$  for different amplitudes of the initial noise. It is clearly visible that for low initial noise (solid line) the maximum is higher and the time until the boundary layer starts depleting is longer than for high initial noise (dotted and dashed line). This is the case because the most unstable mode in the system needs more time to grow to a sufficiently high value the lower the initial noise is.

Independent of the initial condition, at a time of  $\hat{\tau} \approx 30$ , all simulations have reached a boundary layer depth of  $L' \approx 0.2$ . The late-time behaviour of  $L'$  shown in fig. 8 **D** shows that the depth of the boundary layer keeps being independent of the initial condition, with a slight upward trend, which can be explained by the increasing overall amount of salinity in the system. We note that  $L'(\hat{\tau})$  does not show the pronounced oscillations depicted in fig. 7 **B**. This is because the salinity distributions were averaged both over the  $X$ -axis as well as over ensembles of at least 9 runs before calculating  $L'(\hat{\tau})$ . This also indicates that the phase of the oscillations which are observed in a single run is independent of the initial conditions.

## 5. Non-uniform boundary condition and phase-locking

Our modelling aims to provide a mechanism, which can drive pattern formation in salt deserts. We propose, that this mechanism is the buoyancy-driven convection of saline water in the soil below the salt crust on the surface and that the horizontal salinity gradients, which are caused by the convective dynamics and can be measured in the field (Lasser *et al.* 2019), are linked to the growth of ridges in the salt crust. In nature, the growth of ridges takes several weeks to several months. Therefore, the underground dynamics need to stay stationary long enough for the patterns to grow on the surface.

Space-time diagrams of the salinity distribution, as displayed in fig. 6 **B** for one exemplary simulation run, allow for a qualitative assessment of plume positions. As the dynamics unfold, plumes merge in a typical herring-bone-like pattern into a few large plumes and the position of these large plumes fluctuate with time. This coarsening process can also be observed in supplementary movies S2 and S3. We conclude that on its own, the buoyancy-driven convection will not suffice to support pattern formation on the surface, as the convective dynamics do not remain stationary for long.

Following this finding, we propose a feedback mechanism that links the convective dynamics to the crust at the surface. One way to simulate such a feedback mechanism is to modify the top boundary condition for the fluid velocity of  $U_Z(X)$ . So far, the fluid velocity has been a uniform  $U_Z(X) = U_Z^0$ . From now on, we will investigate a non-uniform boundary condition  $U_Z(X) = U_Z^0 - A_m \cdot \cos(k_m X)$ . This corresponds to a sinusoidal modulation of the fluid velocity with a modulation wavenumber  $k_m$  and a modulation amplitude  $A_m$ . In nature, the fluid velocity at the top boundary corresponds

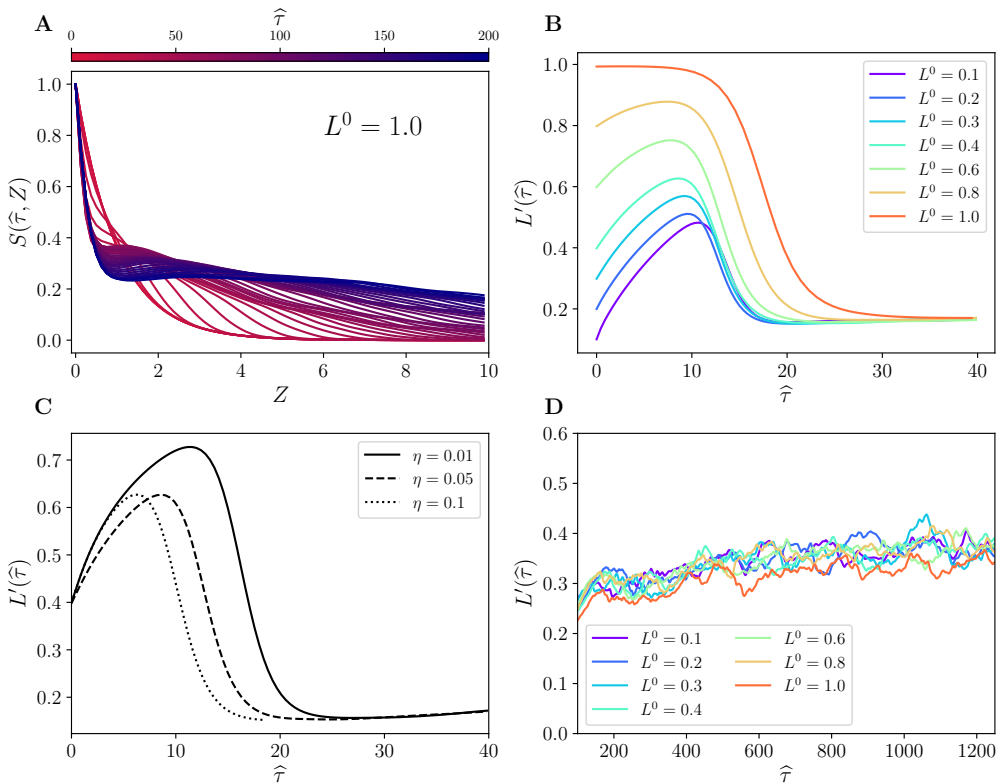


FIGURE 8. Development of the boundary layer thickness  $L'$  at early times for different initial conditions  $L^0$ . Salinity distributions were averaged horizontally and over ensembles of 9-11 simulations run at  $Ra = 100$ . **A** Early time development of the boundary layer thickness  $L'$  in a simulation with initial condition  $L^0 = 1.0$ . **B** Early time development of the boundary layer thickness  $L'$  for different initial conditions  $L^0$ . **C** Time development of the boundary layer thickness starting with  $L^0 = 0.4$  for different initial noise amplitudes  $\eta$ . **D** Late time development of  $L'$  for simulations started at the same initial conditions as in **C**.

to the rate at which fluid evaporates from the surface and modulation of the evaporation rate can be interpreted as the salt crust partially inhibiting evaporation.

In fig. 9 **A** we show space-time diagrams for four different modulation wavenumbers at the same modulation amplitude  $A_m = 1.0$  (see also supplementary movies S4 – S7). It is evident that the downwelling plumes originate at the minima of the velocity profile  $U_Z(X)$ . The plumes then remain locked at the position of the minima for some time, before the order breaks down and the dynamics return to a state which resembles a system with a uniform boundary condition.

We can quantify the spatial alignment of the downwelling plumes by introducing the order parameter  $\xi(\hat{\tau})$

$$\xi(\tau) = \frac{1}{N(\hat{\tau})} \cdot \sum_{i=1}^{N(\hat{\tau})} -\cos(k_m X_i(\hat{\tau})) , \quad (5.1)$$

where  $N(\hat{\tau})$  is the number of plumes at a given point in time and  $X_i(\hat{\tau})$  is the horizontal position of these plumes in space. If  $\xi = 1$ , the plumes existing in the system at time  $\hat{\tau}_i$  and depth  $Z_i$  are aligned to the positions of the minima in  $U_Z(X)$ . If  $\xi = -1$ , the plumes

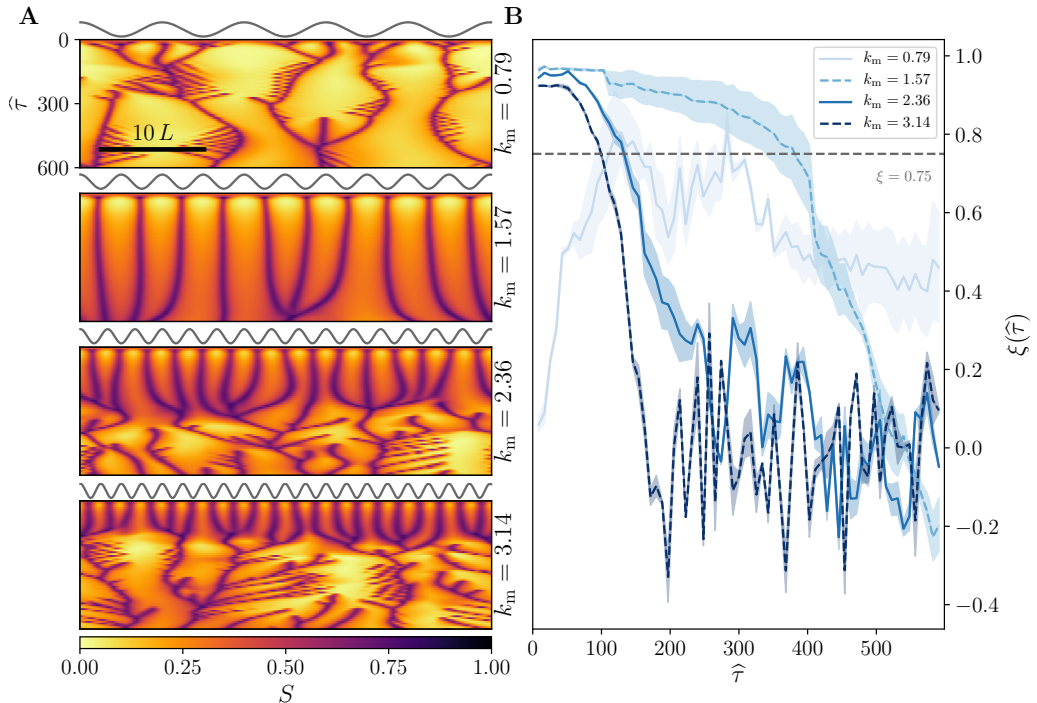


FIGURE 9. Phase-locking of the dynamics to the modulated boundary condition. **A** Space-time diagrams of four exemplary simulations with  $k_m \in [0.79, 1.57, 2.36, 3.14]$  and  $Ra = 100$ ,  $A_m = 1$ . **B** Development of the order parameter  $\xi$  with re-scaled time  $\hat{\tau}$  for the same three modulation wavenumbers. The wavenumbers needed to calculate  $\xi$  were measured at a depth of  $Z = -1$ . Values are averages and standard deviations for ensembles of five simulation runs each.

are anti-aligned and if  $\xi = 0$  there is on average no alignment of plumes in the system. In fig. 9 **B**, we show the development of  $\xi$  as the re-scaled time increases for the four modulation wavenumbers shown in fig. 9 **A**.

Fig. 9 also reveals that the time the plumes stay synchronised with the positions of the minima depends on the modulation wavenumber  $k_m$ . To quantify this dependence, we define the phase-locking time  $T_\phi$  as the time it takes for the order parameter to drop below  $\xi = 0.75$  (grey line in fig. 9 **B**). We measure this time for a selection of modulation amplitudes and wavenumbers. Results are shown in fig. 10. It is clearly visible that the phase-locking time  $T_\phi$  increases with amplitude. Furthermore, it has a pronounced maximum at wavenumbers in the range of  $k_m = 1.3$  to  $1.9$  for modulation amplitudes larger than  $A_m = 0.3$ . This matches the wavelength of polygonal salt ridge patterns observed in nature very well (Lasser *et al.* 2019).

## 6. Evaporation rate modulation in nature

In the following, we want to link the spatial order in the system dynamics to the feedback introduced by modulation of evaporation rate in the field. To this end, we will investigate the time scales of pattern growth as well as the variations of temperature and humidity below ridges, which influence the evaporation rate in the field.

An exemplary field site - Owens Lake - which expresses well pronounced polygonal patterns in the salt crust covering the dry lake-bed was characterised by Lasser *et al.* (2019). Rayleigh numbers at Owens Lake correspond to vigorously convecting systems

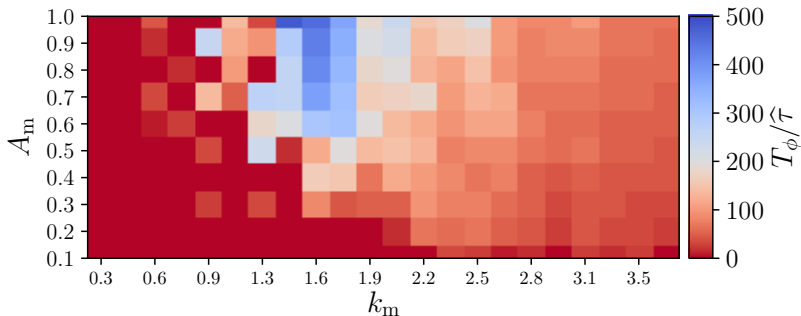


FIGURE 10. Phase-locking time  $T_\phi(A_m, k_m)$  for several modulation amplitudes  $A_m$  and modulation wavenumbers  $k_m$ . Red corresponds to  $T_\phi < 200\hat{\tau}$ , grey to  $T_\phi = 200\hat{\tau}$  and blue to  $T_\phi > 200\hat{\tau}$  respectively. Values for  $T_\phi$  were measured in a single simulation run at  $Ra = 100$  respectively.

with  $Ra > 500$  (Lasser *et al.* 2019) in almost all cases. The median  $Ra$  at Owens Lake is 3700 and the natural time is  $T \approx 262$  days (Lasser *et al.* 2019). For the median Rayleigh number, one year corresponds to  $5100\hat{\tau}$ . Ridge growth of approximately 2.5 cm over the course of two weeks (approximately  $200\hat{\tau}$ ) has been observed (see supplementary movie S8). Therefore, we conclude that a phase-locking time greater than  $200\hat{\tau}$  is enough to support substantial pattern growth in nature. By the time ridges have started to protrude from the flat salt crust, more complete feedback including wicking of fluid through the ridge is likely to take over.

Fig. 10 shows that for moderate modulation amplitudes, only a modulation wavenumber  $1.3 \geq k_m \geq 2.2$  provides reliable and long enough phase-locking for ridges to grow. This is consistent with measurements of  $k$  from several salt pans (Lasser *et al.* 2019). Therefore, phase locking could be a mechanism to stabilise the patterns in nature. We expect that the presence of a salt crust or ridge can inhibit the evaporation of water through the crust to *some* degree but not completely prohibit it.

Temperature and humidity are the main parameters (next to salt concentration and air movement) controlling evaporation from a salt pan. We attempted to estimate the influence of ridges on the micro-climate at crust level by embedding sensors in several ridges of polygons found in nature and tracking temperature and humidity over several days. Measurements were conducted during a field campaign to Owens Lake (CA) in November and December 2016. See the thesis by Lasser (2019) for further details about the field sites. For temperature and humidity measurements, we used HiTemp140 and RHTemp1000IS data loggers, which measured temperatures and relative humidity with a precision of  $\pm 0.01^\circ\text{C}$  and  $\pm 0.1\%$  respectively.

In fig. 11 we show temperature and humidity measurements from sensors placed inside a salt ridge and in the centre of a polygon. The measurements were taken over the course of a week during a field campaign to Owens Lake in winter 2016. In fig. 11 **A**, diurnal fluctuations of temperature between about  $10^\circ\text{C}$  at 2:00 PM and about  $0^\circ\text{C}$  at 6:00 AM are clearly visible. Maximum temperatures during the day are similar between the centre and ridge. Temperatures inside the ridge, however, seem to drop faster and lower at night. The temperature difference is about  $2^\circ\text{C}$  and can be explained by the ridges shading the surface area below them from sunlight. Fig. 11 shows the development of the relative humidity over the course of a week. The relative humidity measured inside the ridge is equal (on the first, third and sixth day) or by up to higher 15% higher (on the second, fourth and fifth day). Humidity differences are most pronounced during nights

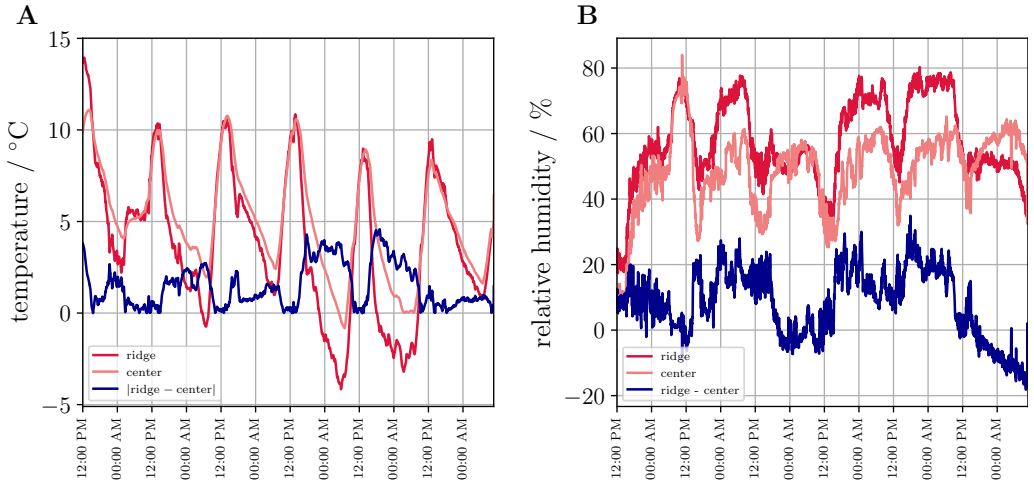


FIGURE 11. Temperature and humidity measures from two salt polygons at Owens Lake, conducted in winter 2016. **A**: temperature measured inside and outside a salt ridge of the same polygon. **B**: humidity measured inside and outside a salt ridge of two polygons about two kilometres apart.

and mornings but are preserved to some extent over the course of the day. The difference in relative humidity can be explained by trapping of air below the ridges. Both reduced temperature and increased relative humidity inhibit evaporation from the surface area below a salt ridge and could serve as the feedback mechanism proposed above, which modulates the evaporation rate.

## 7. Summary

We have presented a numerical study of buoyancy-driven convection in a porous medium, in which we study the characteristics of the ensuing dynamics with changing Rayleigh number and time. Our study is inspired by the situation below an evaporating salt pan, where the dynamics in the underground are suspected to give rise to the emergence of regular polygonal patterns at the surface (Lasser *et al.* 2019). In this context, we investigate (1) the conditions necessary for the system to become unstable and the transient behaviour of the convective dynamics after onset, (2) the wavenumber  $k$  of the downwelling plumes realised by the system and its development in time, and (3) the possible impact of feedback on the dynamics, caused by a growing salt crust at the surface.

We complement the work of Wooding (1960*a*) and van Duijn *et al.* (2002) by calculating the stability criteria and neutral stability curve for both a constant pressure as well as a constant through-flow boundary condition at the surface, following a novel semi-analytical approach. We extend this analysis by also calculating the most unstable mode  $k(Ra)$ .

Similar to Slim (2014), we find that the dynamics undergo several regimes. We characterise the re-initiation regime, where small proto-plumes emerge at the top boundary in between larger plumes, as a dynamical steady state of the system. While the maximum plume velocity realised by the system in the dynamical steady state depends on  $Ra$ , the time to reach the steady state approaches a constant value for  $Ra > 500$ .

The dynamical steady state is characterised by the width of a boundary layer of high salinity. The thickness of the boundary layer in the dynamical steady state oscillates

around a constant value as salinity builds up through evaporation at the surface until the boundary layer is wide enough to support the emergence of new proto-plumes. The mean boundary layer thickness first increases with  $Ra$  and approaches a constant value for  $Ra > 400$ .

The emerging proto-plumes are quickly drawn into large downwelling plumes that stay rather stable in space. The spacing of these large plumes does depend on  $Ra$  but the dependence weakens as  $Ra$  increases. The wavelength corresponding to the wavenumbers in the coarsened system fits the wavelength of the salt polygon patterns observed in nature.

These results indicate that the dynamics realised in a vigorously convecting system are robust to changes in  $Ra$  for Rayleigh numbers far enough away from  $Ra_c$ . This robustness is a necessary feature to explain the mechanism driving salt polygon emergence in nature, as these patterns occur in areas with vastly different Rayleigh numbers (Lasser *et al.* 2019).

Regions of high salinity (e.g. downwelling plumes) are suspected to template the growth of salt ridges at the surface (Lasser *et al.* 2019). As ridges grow, the salt crust at the surface of the porous medium is not uniform anymore and an impact on the previously uniform evaporation at the surface is expected. The influence of ridges on the evaporation rate is also supported by data measured in the field, showing a difference in temperature and air humidity below ridges, as compared to salt polygon centres.

To model the feedback mechanism between the crust and underground dynamics, we also simulated a boundary with a sinusoidal modulation of the fluid through-flow. We find that for a certain range of modulation wavenumbers and amplitudes, the inhomogeneous boundary condition is able to pin the otherwise slowly fluctuating positions of the downwelling plumes in place. This is a necessary condition to support the growth of salt ridges at the surface and the modulation wavenumbers that yield the strongest pinning are consistent with the pattern wavenumbers observed in nature.

Our improved understanding of the temporal and spatial dynamics of buoyancy-driven convection below an evaporating salt pan, therefore, supports the claim that the polygonal patterns often observed on the surface of such pans are caused by convective dynamics. This is in contrast to the existing explanations of Christiansen (1963) and Krinsley (1970), who suspected that the driving mechanism is a folding or cracking of the salt crust.

## Appendix A. Numerical simulation

We implemented a two-dimensional finite-difference model of an evaporating salt lake, based on the non-dimensional equations given in Eqs. (2.8)–(2.10). This uses a pseudo-spectral approach and a stream function-vorticity representation, similar to Chen & Meiburg (1998a); Ruith & Meiburg (2000); Riaz & Meiburg (2003), a sixth-order compact finite difference scheme to compute spatial derivatives and an explicit fourth-order Runge-Kutta scheme for time-stepping.

### *Model setup*

The numerical model simulates a two-dimensional ( $X, Z$ ) area of length  $L$  in the  $X$ -direction and height  $H$  in the  $Z$ -direction. For the salinity  $S$  and flux  $\mathbf{U}$  we assume periodic boundary conditions in the  $X$ -direction. The relative salinity  $S = 1$  at the top boundary ( $Z = 0$ ), and  $S = 0$  at the lower boundary ( $Z = -H$ ). At  $Z = 0$  surface evaporation is modelled as a boundary condition on  $U_Z$ . To allow for a modulation in evaporation rate  $U_Z = 1 - A_m \cos(k_m X)$  there, where  $A_m$  represents the strength of the

modulation and  $k_m$  its wavenumber; for constant evaporation,  $A_m = 0$ . In all cases the average value of  $U_Z$  at the surface is 1. At the bottom boundary,  $Z = -H$ , fluid recharge is assumed to be uniform, such that  $U_Z = 1$  there.

We use potential functions to reformulate the equations of porous media flow, following Ruith & Meiburg (2000); Riaz & Meiburg (2003). For a two-dimensional and incompressible flow the flux  $\mathbf{U}$  is related to the Lagrange stream function (de Lagrange 1781; Kundu *et al.* 2015)  $\psi$  by  $\mathbf{U} = (\partial_Z \psi, -\partial_X \psi)$ . The vorticity,  $\omega = \partial_X U_Z - \partial_Z U_X$ , is then given by the Poisson equation,

$$\nabla^2 \psi = -\omega. \quad (\text{A } 1)$$

Taking the curl of Darcy's Law, Eq. (2.10), allows us to eliminate the pressure term, as  $\nabla \times (\nabla P) = 0$ , and solve for the vorticity as

$$\omega = -Ra \partial_X S. \quad (\text{A } 2)$$

Finally, the salt mass balance of Eq. (2.9) can be written as

$$\partial_\tau S = (\partial_X \psi)(\partial_Z S) - (\partial_Z \psi)(\partial_X S) + \partial_X^2 S + \partial_Z^2 S. \quad (\text{A } 3)$$

To solve Eqs. (A 1) – (A 3) we need boundary conditions for the stream function  $\psi$  and vorticity  $\omega$ . The constraints on flow give  $\partial_X \psi = -1 + A_m \cos(k_m X)$  at  $Z = 0$  and  $\partial_X \psi = -1$  at  $Z = -H$ . These inhomogeneous boundary conditions can be accounted for by taking  $\psi = \psi' + \Psi$ , where

$$\psi' = -X + \frac{A_m}{k_m} \sin(k_m X) \cos^2\left(\frac{\pi Z}{2H}\right), \quad (\text{A } 4)$$

such that  $\partial_X \Psi = 0$  at both  $Z = 0$  and  $Z = -H$ . The constant salinity conditions correspond to a vanishing vorticity,  $\omega = 0$ , at both these surfaces. As an initial condition we use

$$S_0 = \frac{e^Z - e^{-H}}{1 - e^{-H}}, \quad (\text{A } 5)$$

which is the steady-state solution of the salinity when  $A_m = 0$ . Following Riaz & Meiburg (2003) we perturb this by adding random fluctuations into the initial salinity. To do so we generate random numbers  $f(X, Z)$ , uniformly distributed in  $[-1, 1]$ , for all grid points. In order to avoid artifacts in derivatives, these are then convolved with a Gaussian function of width  $\sigma = 3$  grid cells, such that

$$S' = \gamma f(X, Z) * e^{-\frac{x^2+z^2}{\sigma^2}}, \quad (\text{A } 6)$$

where  $\gamma$  gives the magnitude of the perturbation. The initial salinity distribution is then  $S = S_0 + S'$ , at  $\tau = 0$ .

### Implementation

To numerically solve the governing equations of the simulation we largely follow the implementation described by Riaz & Meiburg (2003); Ruith & Meiburg (2000). Specifically, at each time step we: (i) compute derivatives in the  $X$ -direction by first making use of a Fourier transform; (ii) compute derivatives in the  $Z$ -direction by using a compact finite difference scheme (Lele 1992); and (iii) use an explicit fourth-order Runge-Kutta scheme for the time-integration of equation (A 3).

The simulation is performed on a grid of  $M \times N$  points at positions  $(x_m, z_n)$ . The grid spacings  $\Delta X$  and  $\Delta Z$  are of order  $\mathcal{O}(0.02)$ , which is small enough to represent all

	$\alpha_0$	$\alpha_1$	$a_1$	$a_2$	$a_3$	$a_4$	$a_5$	$a_6$		$b_1$	$b_2$	$b_3$	$b_4$	$b_5$	$b_6$
interior		1/3	14/9	1/9											
node 0	5		197/60	-5/12	5	-5/3	5/12	-1/20							
node 1	3/4	1/8	-43/96	-5/6	9/8	1/6	-1/96								
interior	12/97	-1/194	120/7												
boundary	11/12	-131/4	177/16	-507/8	783/8	-201/4	81/16	-3/8							

TABLE 2. Coefficients for sixth order compact finite difference schemes used in the numerical simulations, following Lele (1992); Tyler (2007). The  $\alpha$  and  $a$  terms are used to calculate first derivatives in  $Z$ , and  $\beta$  and  $b$  terms are used for second derivatives.

relevant length-scales. The time step  $\Delta\tau$  follows the CFL-condition (Courant *et al.* 1928)

$$C = \frac{U_{\max} \Delta\tau}{\Delta X} \leq C_0,$$

where  $U_{\max}$  is the maximum speed occurring at that time, and where we set  $C_0 = 0.1$ .

*Derivatives in X-direction:* We employ Fourier expansions, with coefficients

$$\widehat{\Psi}_\xi(z_n) = \frac{1}{M} \sum_{m=1}^M \Psi(x_m, z_n) e^{-2\pi i \xi x_m / L} \quad (\text{A } 7)$$

and analogous expressions for  $\widehat{\psi}'_\xi$  and  $\widehat{\omega}_\xi$ , where  $\xi$  can take integer values between  $\pm M/2$ . In terms of these Fourier coefficients Eq. (A 1) may be written as

$$\left(\frac{2\pi i \xi}{L}\right)^2 \widehat{\Psi}_\xi + \partial_Z^2 \widehat{\Psi}_\xi = -\widehat{\omega}_\xi - \widehat{\omega}_{\xi 0}. \quad (\text{A } 8)$$

where  $\widehat{\omega}_\xi$  are calculated at each time step by a similar transformation of Eq. (A 2), and where  $\widehat{\omega}_{\xi 0} = \nabla^2 \widehat{\psi}'_\xi$  are constant in time and arise from the boundary conditions.

*Derivatives in Z-direction:* To solve the system of equations given by Eq. (A 8) we computed  $\partial_Z^2 \widehat{\Psi}_\xi(z_n)$  following the implicit sixth-order compact finite difference scheme presented by Carpenter *et al.* (1993). The  $N$  linear differential equations can be described by two matrices such that

$$A_{\text{left}} \partial_Z^2 \widehat{\Psi}_\xi(z_n) = A_{\text{right}} \widehat{\Psi}_\xi(z_n) \quad \Rightarrow \quad \partial_Z^2 \widehat{\Psi}_\xi(y_n) = (A_{\text{left}}^{-1} A_{\text{right}}) \widehat{\Psi}_\xi(z_n).$$

To construct the matrices  $A_{\text{left}}$  and  $A_{\text{right}}$ , we use the coefficients  $\alpha_i$ ,  $\beta_i$ ,  $a_i$  and  $b_i$  listed in Table 2, as calculated by Tyler (2007). At each time step we then solve for the Fourier components  $\widehat{\psi}$ , which are inverted to give the stream function  $\psi(x_m, z_n)$ . The flux  $\mathbf{U}$  is then calculated from the stream function by again using an implicit sixth-order compact finite difference scheme for the spatial derivatives. Coefficients for the first and second order derivatives of interior and boundary points are listed in Table 2.

*Time-integration:* To update the salinity field via Eq. (A 3) we used a fourth-order Runge-Kutta scheme, and the coefficients given for example by Süli (2003, p. 352). For spatial derivatives we again use an implicit sixth-order compact finite difference scheme.

## Validation

The model was validated by comparison with the results of the linear stability analysis. A similar approach is used in Ruith & Meiburg (2000); Riaz & Meiburg (2003); Chen & Meiburg (1998a); Tan & Homsy (1988). For this, instead of Eq. (A 6) we perturb our initial conditions with

$$S' = -\gamma Z \left( \frac{e^Z - e^{-H}}{1 - e^{-H}} \right) \cos(kX).$$

This perturbation is consistent with the constant salinity boundary conditions, and affects only a single wavenumber  $k$ . We use an initial amplitude of  $\gamma = 1 \cdot 10^{-5}$ , and monitor the growth of the perturbed mode over time. A growth rate  $\alpha(k, Ra)$  is then fit to the initial exponential growth phase of the simulation. Results agree with the theoretical results to within a relative error of  $10^{-2}$ , as was shown in Fig. 3 B.

## REFERENCES

- BOUFADEL, M.C., SUIDAN, M.T. & VENOSA, A.D. 1999 Numerical modeling of water flow below dry salt lakes: effect of capillarity and viscosity. *Journal of Hydrology* **221** (1), 55–74.
- BRIERE, PETER R 2000 Playa, playa lake, sabkha: Proposed definitions for old terms. *J. Arid Environ.* **45** (1), 1–7.
- BRUNNER, PHILIP, BAUER, PETER, EUGSTER, MARTIN & KINZELBACH, WOLFGANG 2004 Using remote sensing to regionalize local precipitation recharge rates obtained from the Chloride Method. *J. Hydrol.* **294** (4), 241–250.
- BRYANT, ROBERT G 2003 Monitoring hydrological controls on dust emissions: preliminary observations from etosha pan, namibia. *Geogr. J* **169** (2), 131–141.
- BRYANT, R. G. & RAINEY, M. P. 2002 Investigation of flood inundation on playas within the zone of chotts, using a time-series of AVHRR. *Remote Sensing of Environment* **82** (2-3), 360–375.
- BUSSE, F. H. & JOSEPH, D. D. 1972 Bounds for heat transport in a porous layer. *Journal of Fluid Mechanics* **54** (3), 521–543.
- CARPENTER, MARK H., GOTTLIEB, DAVID & ABARBANEL, SAUL 1993 The stability of numerical boundary treatments for compact high-order finite-difference schemes. *Journal of Computational Physics* **108** (2), 272–295.
- CHEN, CHING-YAO & MEIBURG, ECKART 1998a Miscible porous media displacements in the quarter five-spot configuration. part 1. the homogeneous case. *J. Fluid Mech.* **371**, 233–268.
- CHEN, CHING-YAO & MEIBURG, ECKART 1998b Miscible porous media displacements in the quarter five-spot configuration. part 2. effect of heterogeneities. *Journal of Fluid Mechanics* **371**, 269–299.
- CHRISTIANSEN, F. W. 1963 Polygonal fracture and fold systems in the salt crust, Great Salt Lake Desert, Utah. *Science* **139** (3555), 607–609.
- COURANT, R., FRIEDRICHS, K. & LEWY, H. 1928 ber die partiellen differentialgleichungen der mathematischen physik. *Mathematische Annalen* **100**, 32–74.
- CROSS, MICHAEL & GREENSIDE, HENRY 2009 *Pattern Formation and Dynamics in Nonequilibrium Systems*. Cambridge University Press.
- DARCY, HENRY 1856 Les fontaines publique de la ville de dijon. *Dalmont, Paris* **647**.
- VAN DUJN, C. J., PIETERS, G. J. M., WOODING, R. A. & VAN DER PLOEG, A. 2002 Stability criteria for the vertical boundary layer formed by throughflow near the surface of a porous medium. In *Environmental Mechanics: Water, Mass and Energy Transfer in the Biosphere*, pp. 155–169. American Geophysical Union.
- ELDER, J. W. 1967 Steady free convection in a porous medium heated from below. *Journal of Fluid Mechanics* **27** (01), 29.
- GILL, THOMAS E. 1996 Eolian sediments generated by anthropogenic disturbance of playas:

- Human impacts on the geomorphic system and geomorphic impacts on the human system. *Geomorphology* **17** (1), 207 – 228.
- GRAHAM, MICHAEL D. & STEEN, PAUL H. 1994 Plume formation and resonant bifurcations in porous-media convection. *Journal of Fluid Mechanics* **272**, 6790.
- GROENEVELD, D.P., HUNTINGTON, J.L. & BARZ, D.D. 2010 Floating brine crusts, reduction of evaporation and possible replacement of fresh water to control dust from Owens Lake bed, California. *J. Hydrol.* **392** (3), 211 – 218.
- HANDFORD, C. ROBERTSON 2003 Estimated ground-water discharge by evapotranspiration from Death Valley, California, 19972001. *U.S. Geol. Survey* **3**.
- HARFASH, A. J. 2013 Three-dimensional simulations for convection problem in anisotropic porous media with nonhomogeneous porosity, thermal diffusivity, and variable gravity effects. *Transport in Porous Media* **102** (1), 43–57.
- HEWITT, DUNCAN R., NEUFELD, JEROME A. & LISTER, JOHN R. 2014 High rayleigh number convection in a porous medium containing a thin low-permeability layer. *Journal of Fluid Mechanics* **756**, 844869.
- HEWITT, DUNCAN R., NEUFELD, JEROME A. & LISTER, JOHN R. 2012 Ultimate regime of high rayleigh number convection in a porous medium. *Phys. Rev. Lett.* **108**, 224503.
- HEWITT, DUNCAN R., PENG, GUNNAR G. & LISTER, JOHN R. 2019 Buoyancy-driven plumes in a layered porous medium. *Journal of Fluid Mechanics* **883**.
- HEWITT, DUNCAN R., PENG, GUNNAR G. & LISTER, JOHN R. 2020 Buoyancy-driven plumes in a layered porous medium. *J. Fluid Mech.* **883**, A37.
- HOMSY, GEORGE M & SHERWOOD, ALBERT E 1976 Convective instabilities in porous media with through flow. *AIChE Journal* **22** (1), 168–174.
- HORTON, C. W. & ROGERS, F. T. 1945 Convection currents in a porous medium. *Journal of Applied Physics* **16** (6), 367–370.
- KOEKOEK, ROELOF & SWARTTOUW, RENE F 1998 The askey-scheme of hypergeometric orthogonal polynomials and its q-analogue.
- KRINSLEY, D. 1970 A geomorphological and paleoclimatological study of the playas of Iran. Part 1. *U.S. Geol. Survey* **CP 70-800**.
- KUNDU, PIJUSH, COHEN, IRA & DOWLING, DAVID 2015 *Fluid Mechanics*, 6th edn. Academic Press.
- DE LAGRANGE, JOSEPH LUIS 1781 Mmoir sur la thorie du mouvement des fluides. *Oevres comltes* **4**, 695–748.
- LAPWOOD, E. R. 1948 Convection of a fluid in a porous medium. *Mathematical Proceedings of the Cambridge Philosophical Society* **44** (4), 508521.
- LASSER, JANA 2019 Geophysical pattern formation of salt playa. PhD thesis, Georg-August-University Göttingen.
- LASSER, J., NIELD, J.M., ERNST, M., KARIUS, V., WIGGS, G.F.S. & GOEHRING, L. 2019 Salt polygons are caused by convection. *ArXiv* .
- LELE, SANJIVA K 1992 Compact finite difference schemes with spectral-like resolution. *Journal of computational physics* **103** (1), 16–42.
- LI, QIAN, CAI, WEIHUA, LI, FENG-CHEN, LI, BINGXI & CHEN, CHING-YAO 2019 Miscible density-driven flows in heterogeneous porous media: Influences of correlation length and distribution of permeability. *Physical Review Fluids* **4** (1).
- LOODTS, V., RONGY, L. & DE WIT, A. 2014 Impact of pressure, salt concentration, and temperature on the convective dissolution of carbon dioxide in aqueous solutions. *Chaos: An Interdisciplinary Journal of Nonlinear Science* **24** (4), 043120.
- LOWENSTEIN, TIM K. & HARDIE, LAWRENCE A. 1985 Criteria for the recognition of salt-pan evaporites. *Sedimentology* **32** (5), 627–644.
- MARTICORENA, B. & BERGAMETTI, G. 1995 Modeling the atmospheric dust cycle: 1. design of a soil-derived dust emission scheme. *Journal of Geophysical Research* **100** (D8), 16415–16430.
- METZ, BERT, DAVIDSON, OGUNLADE, CONINCK, HELEEN DE, LOOS, MANUELA & MEYER (EDS.), LEO 2005 IPCC special report on carbon dioxide capture and storage. *Tech. Rep.*. Cambridge University Press, New York, NY (United States).
- NIELD, J. M., BRYANT, R. G., WIGGS, G. F. S., KING, J., THOMAS, D. S. G., ECKARDT,

- F. D. & WASHINGTON, R. 2015 The dynamism of salt crust patterns on playas. *Geology* **43** (1), 31–34.
- OTERO, JESSE, DONTCHEVA, LUBOMIRA A., JOHNSTON, HANS, WORTHING, RODNEY A., KURGANOV, ALEXANDER, PETROVA, GUERGANA & DOERING, CHARLES R. 2004 High-rayleigh-number convection in a fluid-saturated porous layer. *Journal of Fluid Mechanics* **500**, 263281.
- PELLEW, ANNE & SOUTHWELL, RV 1940 On maintained convective motion in a fluid heated from below. In *Proceedings of the Royal Society of London A: Mathematical, Physical and Engineering Sciences*, , vol. 176, pp. 312–343.
- PHOTOGRAPHERSNATURE 2012 Death valley's badwater salt flats at twilight. [https://en.wikipedia.org/wiki/Badwater\\_Basin#/media/File:Badwater\\_Salt\\_Flats\\_at\\_Twilight.jpg](https://en.wikipedia.org/wiki/Badwater_Basin#/media/File:Badwater_Salt_Flats_at_Twilight.jpg), acceses 2020-01-03.
- PROSPERO, J. M. 2002 Environmental characterization of global sources of atmospheric soil dust identified with the NIMBUS 7 total ozone mapping spectrometer (TOMS) absorbing aerosol product. *Reviews of Geophysics* **40** (1).
- RAUPACH, M. R., GILLETTE, D. A. & LEYS, J. F. 1993 The effect of roughness elements on wind erosion threshold. *Journal of Geophysical Research: Atmospheres* **98** (D2), 3023–3029.
- RIAZ, A & MEIBURG, E 2003 Three-dimensional miscible displacement simulations in homogeneous porous media with gravity override. *J. Fluid Mech.* **494**, 95–117.
- RUIH, MICHAEL & MEIBURG, ECKART 2000 Miscible rectilinear displacements with gravity override. part 1. homogeneous porous medium. *J. Fluid Mech.* **420**, 225–257.
- SHARP, J. M. & SHI, M. 2009 Heterogeneity effects on possible salinity-driven free convection in low-permeability strata. *Geofluids* **9** (4), 263–274.
- SLIM, ANJA C. 2014 Solutal-convection regimes in a two-dimensional porous medium. *Journal of Fluid Mechanics* **741**, 461491.
- SLIM, ANJA C., BANDI, M. M., MILLER, JOEL C. & MAHADEVAN, L. 2013 Dissolution-driven convection in a heleshaw cell. *Physics of Fluids* **25** (2), 024101, arXiv: <https://doi.org/10.1063/1.4790511>.
- SÜLI, ENDRE 2003 *An Introduction to Numerical Analysis*. Cambridge University Press.
- TAN, C. T. & HOMS, G. M. 1988 Simulation of nonlinear viscous fingering in miscible displacement. *The Physics of Fluids* **31** (6), 1330–1338, arXiv: <https://aip.scitation.org/doi/pdf/10.1063/1.866726>.
- TAYLOR, GEOFFREY 1953 Dispersion of soluble matter in solvent flowing slowly through a tube. In *Proceedings of the Royal Society of London A: Mathematical, Physical and Engineering Sciences*, , vol. 219, pp. 186–203.
- TYLER, JONATHAN G 2007 Analysis and implementation of high-order compact finite difference schemes. PhD thesis, Brigham Young University.
- TYLER, SW, KRANZ, S, PARLANGE, MB, ALBERTSON, J, KATUL, GG, COCHRAN, GF, LYLES, BA & HOLDER, G 1997 Estimation of groundwater evaporation and salt flux from owens lake, california, usa. *Journal of Hydrology* **200** (1-4), 110–135.
- VAN DAM, REMKE L., SIMMONS, CRAIG T., HYNDMAN, DAVID W. & WOOD, WARREN W. 2009 Natural free convection in porous media: First field documentation in groundwater. *Geophysical Research Letters* **36** (11).
- WASHINGTON, R., TODD, M., MIDDLETON, N. J. & GOUDIE, A. S. 2003 Dust-storm source areas determined by the total ozone monitoring spectrometer and surface observations. *Annals of the Association of American Geographers* **93** (2), 297–313.
- WOODING, RA 1960a Rayleigh instability of a thermal boundary layer in flow through a porous medium. *Journal of fluid mechanics* **9** (2), 183–192.
- WOODING, ROBIN A 1960b Instability of a viscous liquid of variable density in a vertical heleshaw cell. *J. Fluid Mech.* **7** (4), 501–515.
- WOODING, R. A., TYLER, SCOTT W. & WHITE, IAN 1997 Convection in groundwater below an evaporating salt lake: 1. onset of instability. *Water Resources Research* **33** (6), 1199–1217.